Surgical and Radiologic Anatomy (2019) 41:513–522
https://doi.org/10.1007/s00276-019-02201-2

ANATOMIC VARIATIONS

Cone-beam computed tomography evaluation of the pterygomaxillary fissure and pterygopalatine fossa using 3D rendering programs

Murat Icen[1] · **Kaan Orhan**[2,3]

Received: 14 November 2018 / Accepted: 31 January 2019 / Published online: 6 February 2019

Abstract

Purpose The aim of this study was to investigate the detailed anatomy of the pterygomaxillary fissure (PMF) and pterygopalatine fossa (PPF) and variations therein using three-dimensional (3D) cone-beam computed tomography (CBCT) software.

Methods This study was based on a retrospective evaluation of CBCT scans. A total of 825 CBCT images of patients (448 females, 377 males) who met the inclusion criteria were analyzed. PMF shapes were classified, and morphometric measurements (PMF area and PPF volume) were performed according to age, right/left side, and gender using 3D rendering programs. Maxillary and sphenoid sinus pathologies were also classified to reveal possible correlations between morphometric measurements. Analysis of variance was used for comparisons. Multiple comparisons were assessed using the Bonferroni test. Pearson's test was used to assess correlations between parameters. A p value < 0.05 was considered to indicate statistical significance.

Results Six types of PMF shapes were defined. There were no significant differences in types according to gender, age or sinus pathology. Males had a significantly larger PMF area than females ($p < 0.001$). Left/right comparison of the PMF area revealed that the mean PMF coronal, axial, and sagittal area dimensions were significantly higher on the right side in all patients. Our results also indicated that the PMF area and PPF volume increased significantly after 40 years of age.

Conclusion Various PMF shapes were defined and classified. PMF and PPF dimensions increased with age. Knowledge of these anatomical variations will allow surgeons to avoid damage to the neurovascular structures passing through the area.

Keywords Pterygomaxillary fissure · Pterygopalatine fossa · Morphometry · Anatomy · Cone-beam computed tomography

Introduction

The pterygopalatine fossa (PPF) is a small pyramidal space below the apex of the orbit on the lateral side of the skull [11]. This space is an inverted pyramid-shaped space bound by the junction of the maxilla, palatine, and sphenoid bones [33]. However, using a three-dimensional (3D) printing model of PPF, Bannon et al. demonstrated that the true shape of the PPF is more complex than a simple inverted pyramid [3]. Situated between the infratemporal fossa laterally and the nasopharynx medially, it functions as a neurovascular conduit [11]. This space is located at the crossroads between the neurocranium and viscerocranium; deep and outside the skull base [7]. The body of the sphenoid forms the roof, the posterior boundary includes the root of the pterygoid process and the adjoining anterior surface of the greater wing of the sphenoid, and the anterior boundary is the superomedial part of the infratemporal surface (posterior wall) of the maxilla. The perpendicular plate of the palatine bone, with its orbital and sphenoidal processes, forms the medial boundary, and the pterygomaxillary fissure (PMF) is the lateral boundary [11].

The PPF communicates with the middle cranial fossa via two openings in its posterior wall: the foramen rotundum (round foramen), which carries the maxillary nerve, and the

✉ Kaan Orhan
call53@yahoo.com

1 Department of Oral and Maxillofacial Radiology, Faculty of Dentistry, Zonguldak Bülent Ecevit University, Zonguldak, Turkey

2 Department of Dentomaxillofacial Radiology, Faculty of Dentistry, Ankara University, Besevler, Ankara 06560, Turkey

3 OMFS IMPATH Research Group, Department of Imaging and Pathology, Faculty of Medicine, University of Leuven and Oral and Maxillofacial Surgery, University Hospitals Leuven, Leuven, Belgium

pterygoid canal (Vidian canal), which carries the nerve of the pterygoid canal (Vidian nerve). The fossa communicates with the nasal cavity via the sphenopalatine foramen, with the orbit via the medial end of the inferior orbital fissure, and with the infratemporal fossa via the pterygomaxillary fissure, which lies between the back of the maxilla and the pterygoid process of the sphenoid and carries the maxillary artery. It also communicates with the oral cavity via the greater palatine canal, which opens into the posterolateral aspect of the hard palate [11], and with the nasopharynx via the palatovaginal canal [7].

The main contents of the PPF are the third part of the maxillary artery, the maxillary nerve and many of its branches, and the pterygopalatine ganglion [11].

The PMF forms the lateral connection between the PPF and infratemporal fossa. The PMF is the main access to the PPF from the fossa infratemporalis [26]. The maxillary artery enters the PPF from the infratemporal fossa through this fissure. This particular anatomical location is especially important for ear, nose, throat, and maxillofacial surgeons, as the PMF is in an important landmark for Le Fort I osteotomies [11, 12].

Multi-slice computed tomography (CT) has been widely used in maxillofacial imaging, but the major problems with these systems are their cost and large area requirements. Additionally, the dose administered to the patient for maxillofacial examinations is quite high [4, 8, 9].

However, due to developments in medical technology, devices that require less space and operate at lower doses have begun to be produced; cone-beam CT (CBCT) is one such method. Volumetric data of the maxillofacial region can be obtained with this method. The characteristic feature of this method is that it is possible to obtain a higher resolution image with a lower radiation dose than conventional maxillofacial CT [2, 32].

A low radiation dose; shorter scan time; low cost; easy operation; fewer imaging artifacts; beam limitation; axial, sagittal, coronal, and multiplanar sections that allow for interactive imaging; ray casting; and 3D volumetric planning with the obtained images are the main advantages of CBCT [19, 20, 28, 37].

Le Fort I osteotomy, one of the methods used for surgical correction of an abnormal maxilla position, is among the most commonly performed orthognathic surgical procedures [13, 14]. To avoid damage to the maxillary artery during pterygomaxillary separation in Le Fort I osteotomy, the surgeon must have sufficient knowledge of the maxillary artery, PMF, and pterygomaxillary junction as well as their anatomical variations [13, 27].

Moreover, the PMF can be used for maxillary nerve and pterygopalatine ganglion block anesthesia in the treatment of trigeminal neuralgia. It was suggested that the needle should pass through the face and be inserted through the PMF into the PPF to the anterior aspect of the round foramen to achieve successful anesthesia or a maxillary nerve block for trigeminal neuralgia patients [25]. Previous studies have described CT for guided nerve blockage to determine the position of the round foramen and the PMF between the dorsum sellae and the orbital apex prior to the procedure [31]. These studies clearly stated that the anatomy can influence the inventions; hence, a thorough assessment of the PMF and PFF size and shape, with particular focus on lateral access to the maxillary nerve, is crucial for successful interventions [30]. Knowledge of the relevant regional anatomy prior to these interventional procedures helps surgeons to avoid complications, such as failure or insufficient depth of anesthesia, intravascular injection, optic nerve anesthesia or damage, and needle breakage.

Thus, the aim of the current study was to investigate the detailed anatomy of the PMF and PPF, and variations therein, and to evaluate potential correlations of surrounding structures in relation to PMF and PPF anatomy using CBCT.

Materials and methods

In this study, CBCT data of 1000 patients who were referred to the Near East University, Faculty of Dentistry, and Teknodent Imaging Center, between 2011 and 2018 for various reasons were reviewed retrospectively. There was no gender preference in the sample choice.

Ethical approval was obtained from the University Scientific Research Ethics Committee (IRB approval number 18/2011-16). The examiner only examined radiographs and was blinded to all other patient data in the radiographic examination procedure.

Exclusion criteria were as follows: age less than 18 years; a history of trauma to the head or neck; past sinus or skull base surgery; the presence of systemic conditions; the presence of a genetic disorder, syndrome, or congenital anomaly (craniocytosis, hemi-facial microsomia) affecting the head and neck region; and pathology or fractures in the relevant region. Furthermore, only high-resolution tomography scans were included.

After exclusion, CBCT data of 825 patients (448 females, 377 males) who met these criteria were included in the final study group. The patients ranged in age from 18 to 91 years.

Data acquisition and processing

CBCT scans were obtained using a NewTom 3G (Quantitative Radiology S.R.L., Verona, Italy) device. Patients were stabilized in a supine position using specially designed head bands and chin straps positioned with the Frankfort horizontal plane perpendicular to the floor and monitored to ensure that they remained motionless during scanning

(36 s). All images were recorded at 120 kVp, 3–5 mA in a 9-in. imaging area, with an axial slice thickness of 0.3 mm and using isotropic voxels. The X-ray parameters for kV and mA were automatically determined from the scout images. All reconstructions and measurements were made on a 21.3-in. flat-panel color active-matrix thin-film transistor medical display (Nio Color 3MP, Barco, Belgium) with a resolution of 2048 × 1536 at 76 Hz and 0.2115-mm dot pitch operated at 10 bits. The examiner was also permitted to use enhancements and orientation tools, such as magnification, brightness, and contrast, to improve visualization of the landmarks.

To evaluate PMF and PPF anatomy, CBCT axial images were first exported in DICOM file format with a 512 × 512 matrix and imported into Maxilim® version 2.3.0. (Medicim, Sint-Niklass, Belgium). Reconstruction was performed in multiple stages to obtain images diagnostically suitable for landmark identification and 3D reconstruction. 3D-segmented hard tissue surface representations of the maxillary anatomy were rendered in a virtual scene. The PMF was then sculpted out from the 3D-represented image, and the PMF shape was defined according to the study by Acar et al. [1]. Axial, sagittal, and cross-sectional images were reconstructed and fused on 3D representations separately for both sides of the maxilla (Fig. 1).

CBCT data were also transferred to InVivoDental (Version 5, Anatomage, San Jose, CA, USA) software for measurements of the PMF area and PPF volume (Fig. 2). The PMF and PPF were segmented separately. Images that showed the largest right and left PMF borders in the axial, sagittal, and coronal planes were identified in multiplanar reconstruction images. The area measurement tool was selected in these sections, and the fissure edges were followed as closely as possible to mark an enclosed PMF area. The PMF area was calculated from axial, sagittal, and coronal sections separately (Fig. 2). Similarly, the PPF area was sculpted out from 3D images using the same software. Manual segmentation was performed to examine the anatomy of the PPF. After segmentation, PPF volumes were measured automatically using the software airway analysis tool (Fig. 3).

For analysis, the study group was divided into three subgroups according to gender and age. Age groups were

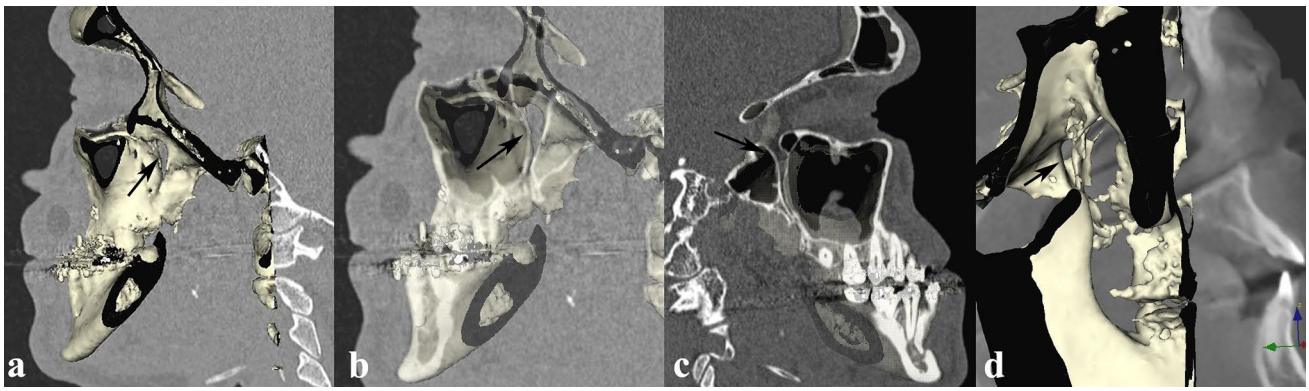

Fig. 1 Three-dimensional (3D) representation and cone-beam computed tomography (CBCT) fused images of the pterygomaxillary fissure (PMF) (arrows) using 3D rendering software. **a, d** 3D-surface rendered image superimposed with the corresponding coronal CBCT slice. **b** Transparent 3D image and coronal CBCT slice in the background. **c** Transparent coronal CBCT slice and 3D image (in the background) were used to visualize the PMF anatomy in detail

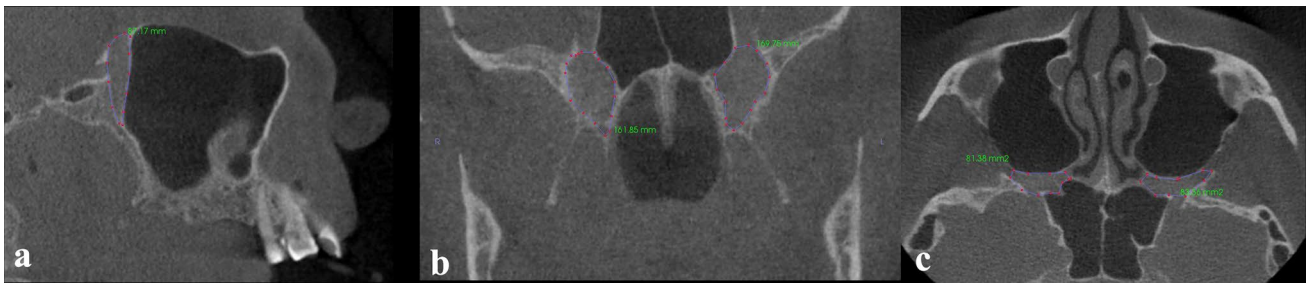

Fig. 2 **a** Sagittal, **b** coronal, and **c** axial CBCT images showing measurement of the PMF area using the corresponding software. Note that after manual tracing, the software calculated the area automatically

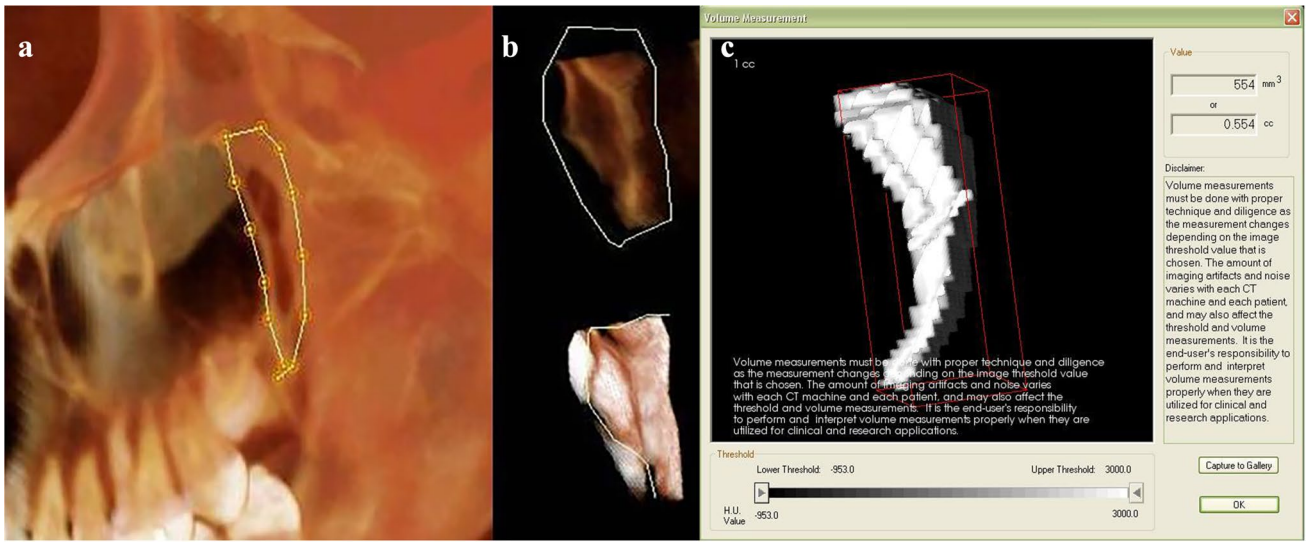

Fig. 3 3D images showing pterygopalatine fossa (PPF) volume measurement. **a** 3D CBCT images were changed to airway mode (to visualize the areas containing air), which was applied automatically using the software. **b** The PPF area was then sculpted out from 3D images, and manual segmentation was performed to evaluate the anatomy of the PPF. **c** After segmentation, PPF volumes were measured automatically using a software airway analysis tool

classified as follows: 18–30, 31–40, 41–50, 51–60, 61–70, 71–80, and 81–91 years.

Patients were also classified according to their maxillary and sphenoid sinus conditions as follows: no pathology, only mucosal thickening (defined as a mucosal thickening of no more than 1 cm), and pathology (such as mucous retention cysts, air/fluid level, sinusitis, etc.). None of the patients had any tumor or trauma that caused a disturbance or expansion of the bony borders of the sinuses.

Statistical methods

The data obtained during this study were analyzed using the SPSS version 21.0 (SPSS, Chicago, IL, USA) software package. All measurements were repeated by the same investigator within 1 month without having obtained the initial results. If any discrepancy emerged, averages were used for analyses. Intraobserver results were statistically evaluated by Wilcoxon matched-pairs signed-ranks test.

Analysis of variance (ANOVA) was used for comparisons. Bonferroni's test was used for multiple comparisons. Pearson's test was used to assess correlations between parameters. Bivariate correlation analysis was used for side (right/left) comparisons of parametric values, and the marginal homogeneity test was applied for right/left comparisons of non-parametric values. The *t*-test was used to evaluate gender differences. Arithmetic mean, standard deviation, and standard error values of the data were determined in Microsoft Excel. A p value < 0.05 was considered statistically significant.

Results

Table 1 shows the PMF shapes identified in this study. In total, six types of PMF shape were defined and identified as types A, B, C, D, E, and F (Fig. 4). The most common PMF shapes on both the left and right sides were C in males and E in females, with B being the least common. Across all study groups, the most common shapes were D on the right side and C on the left side, whereas B was the least common (Table 1). There was no significant difference in types according to gender, age, or sinus pathology ($p > 0.05$) (Table 2).

Table 3 shows the PMF area in all sections. Males had a significantly larger PMF area than females ($p < 0.001$) (Table 3). Left/right comparison of the PMF area revealed that the mean PMF coronal, axial, and sagittal area dimensions were significantly higher on the right side in all patients ($p < 0.001$) (Table 3). Table 4 shows the PPF volume according to gender and location. Significantly larger PPF volumes were found in male patients than in females and on the right side compared with the left side (all $p < 0.001$).

Table 4 shows the PMF dimensions and PPF volumes according to age. The PMF area in all sections and PPF volume tended to increase with age. There were significant differences ($p < 0.001$) between the 18–30-years age group and all other age groups except for the 31–40-years group. The results also indicated that the PMF area and PPF volume increased significantly after 40 years of age. Overall, there were no significant differences in PMF shape, PMF area, and PMF volume according to sinus condition.

Table 1 Distribution and statistical analysis of PMF types by side and gender

	Right			Left			Multiple comparisons			
	Gender		Total	Gender		Total	*p* values			
	Male (1)	Female (2)		Male (3)	Female (4)		1 vs. 2	1 vs. 3	2 vs. 4	3 vs. 4
PMF shape										
A	48 (5.8%)	72 (8.7%)	120 (14.5%)	58 (7.0%)	87 (10.5%)	145 (17.6%)	> 0.05	> 0.05	> 0.05	> 0.05
B	35 (4.2%)	48 (5.8%)	83 (10.1%)	29 (3.5%)	40 (4.8%)	69 (8.4%)	> 0.05	> 0.05	> 0.05	> 0.05
C	88 (10.7%)	82 (9.9%)	170 (20.6%)	96 (11.6%)	72 (8.7%)	168 (20.4%)	> 0.05	> 0.05	> 0.05	> 0.05
D	86 (10.4%)	88 (10.7%)	174 (21.1%)	68 (8.2%)	84 (10.2%)	152 (18.4%)	> 0.05	> 0.05	> 0.05	> 0.05
E	72 (8.7%)	99 (12.0%)	171 (20.7%)	59 (7.2%)	90 (10.9%)	149 (18.1%)	> 0.05	> 0.05	> 0.05	> 0.05
F	48 (5.8%)	59 (7.2%)	107 (13.0%)	67 (8.1%)	75 (9.1%)	142 (17.2%)	> 0.05	> 0.05	> 0.05	> 0.05
Total	377 (45.7%)	448 (54.3%)	825 (100.0%)	377 (45.7%)	448 (54.3%)	825 (100.0%)	> 0.05	> 0.05	> 0.05	> 0.05

p values < 0.05 indicate statistical significance

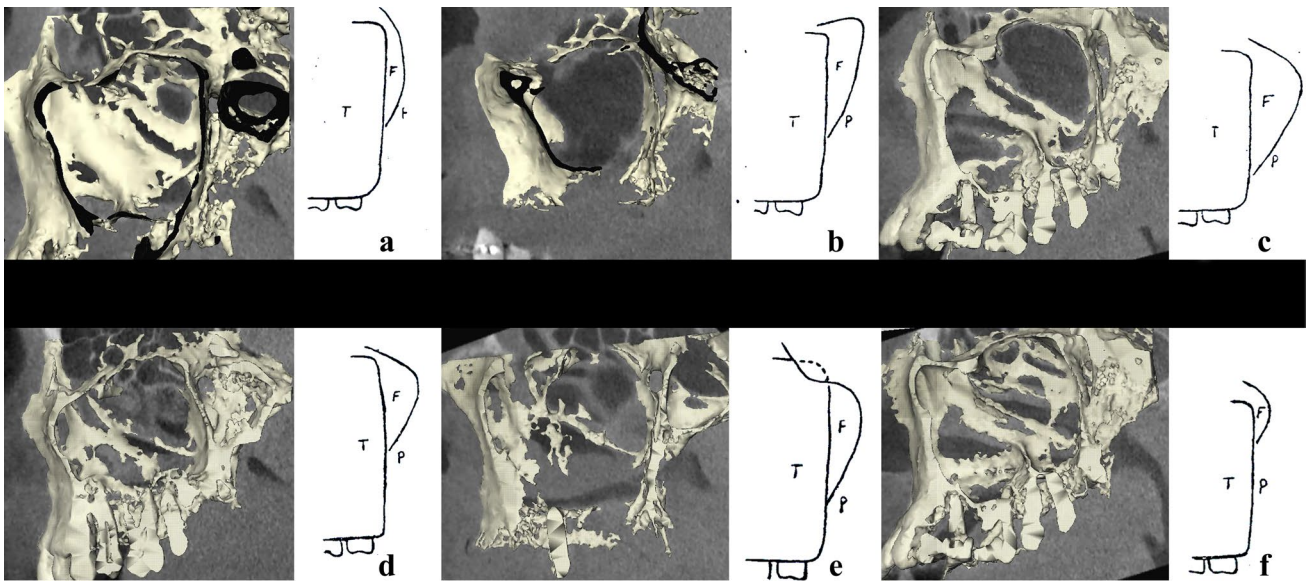

Fig. 4 3D-surface rendered image superimposed with the corresponding coronal CBCT slices of different PMC shapes. In total, six different PMF shapes were identified (**a**–**f**)

Discussion

In the present study, we evaluated variations in PMF shape because a narrow or irregular PMF may lead to difficulties both in diagnosis and in therapeutic injections and surgical procedures. Based on conformational variations in lateral projections, we modified the classification system of Acar et al. [1] and identified six different PMF shapes: A, B, C, D, E, and F. This study also evaluated shape variations in the PMF from cadavers. In the previous study [1], type A was the most common, with a prevalence of approximately 50%, and types F and G were the least common. The authors noted that awareness of these variations in PMF shape may be beneficial considering that the PMF may be accessed when block anesthesia of the major nerves passing from the PPF is required, in surgical oncology, and in cases of pterygopalatine ganglion neuralgia [1]. In the present study, the PMF shape similar to type A was present in 16.1% of subjects, and PMF shapes similar to types F and G were observed in 19.4% and 15.1% of subjects, respectively. Of all the PMF shapes identified in our study, we believe that the narrow type A and narrow, irregular, small type F PMFs may cause difficulties during procedures (Fig. 4).

Puche-Torres et al. [26] described anatomical variations in the PMF in their radiological study according to the measure of width of each craniocaudal third. They evaluated the

Table 2 PMF shapes according to age

	PMF shape (right)						*p* value	Total
	A	B	C	D	E	F		
Age groups (years)								
18–30	41	20	40	31	48	30	> 0.05	210
31–40	17	11	25	20	17	17	> 0.05	107
41–50	18	9	30	25	28	16	> 0.05	126
51–60	24	19	44	60	41	26	> 0.05	214
61–70	16	15	20	27	27	18	> 0.05	123
71–80	2	7	8	10	9	0	> 0.05	36
81–91	2	2	3	1	1	0	> 0.05	9
Total	120	83	170	174	171	107	> 0.05	825
	PMF shape (left)						*p* value	Total
	A	B	C	D	E	F		
Age groups (years)								
18–30	41	18	44	32	37	38	> 0.05	210
31–40	23	4	21	20	18	21	> 0.05	107
41–50	22	8	26	22	31	17	> 0.05	126
51–60	32	18	44	48	37	35	> 0.05	214
61–70	19	13	24	23	19	25	> 0.05	123
71–80	5	7	6	7	6	5	> 0.05	36
81–91	3	1	3	0	1	1	> 0.05	9
Total	145	69	168	152	149	142	> 0.05	825

PMF (upper, middle, and lower) by age, gender, side, and width. In the current study, four types of PMF were reported according to shape. In our study, we evaluated the shape of the PMF three dimensionally and calculated area measurements in the sagittal, axial, and coronal planes, and we included PPF volume measurements.

Moiseiwitsch and Irvine [22] also conducted a cadaver study and determined the length of the PMF by measuring the distance from the deepest point of the buccal sulcus to the peak of the fissure. Their data indicated that the PMF was approximately 3 mm longer in males than in females, which they found to be significant. However, they observed no significant difference in PMF length based on ethnicity [22]. In the current study, the PMF area dimensions were larger in male patients, which can easily be explained by sexual dimorphism. Moreover, in our study, the right side displayed larger dimensions than the left side, although there was no difference in shape. Being aware of this difference, needle penetration for nerve blockage should be performed carefully, especially on the left side, due to dimensional differences.

It may be inferred from these differences between right- and left-side measurements that tumoral spread between the PPF and infratemporal fossa may be asymmetric. Accordingly, spread would be expected to occur more easily and rapidly in areas with larger dimensions regardless of gender. Studies involving larger populations or advanced animal models are needed to evaluate this hypothesis. It should also be kept in mind that the results of population-based studies cannot be generalized; these models and data must be considered specific to the studied population.

Comparisons of PMF area measurements within the decade-based age groups revealed a significant increase in PMF area and PPF volume with age (Table 4). There were significant differences between 18 and 30-years group and all other age groups except for the 31–40-years group ($p < 0.001$). These results indicate that the PMF area increases significantly after 40 years of age.

In our study, an increase in the volume of the right and left PPF was observed as the number of missing teeth increased. As a result of the lack of teeth, maxillary sinus downward sagging is believed to cause a relative increase in volume due to the close proximity of the PPF in the natural direction of the direction of gravity. Postural changes are believed to cause changes in the growth direction of the fossa.

The volume of the PPF increased in patients with maxillary sinus pathology. In the presence of pathology, there was a decline in sinus development due to deterioration of the sinus pneumatization, supporting studies of Moss and Salentijn's [24] functional matrix hypothesis and the study by Dargaud et al. [6]. Kim et al. [15] reported that the increase

Table 3 PMF area measurements in the sagittal, axial, and coronal planes and PPF volume measurements according to side and gender

Gender		RIGHT			LEFT			Multiple comparisons				
		Male (1)	Female (2)	Total	Male (3)	Female (4)	Total	*p* values				
		Mean (SD)	Mean (SD)	Mean (SD)	Mean (SD)	Mean (SD)	Mean (SD)	1 vs. 2	1 vs. 3	2 vs. 3	2 vs. 4	3 vs. 4
Sagittal	PMF area (mm^2)	104.2 (27.7)	90.3 (21.9)	96.7 (25.6)	102.6 (25.5)	90.5 (21.7)	96.0 (24.3)	< 0.001	> 0.05	< 0.001	> 0.05	< 0.001
Axial	PMF area (mm^2)	100.9 (30.8)	90.5 (28.6)	95.4 (29.6)	100.2 (33.9)	88.8 (28.9)	94.8 (31.3)	< 0.001	> 0.05	< 0.001	> 0.05	< 0.001
Coronal	PMF area (mm^2)	104.5 (32.7)	96.9 (28.4)	100.3 (30.6)	103.8 (33.1)	96.1 (29.1)	99.6 (31.2)	< 0.001	> 0.05	< 0.001	> 0.05	< 0.001
Volume	PPF volume (mm^3)	1005.1 (27.7)	919.9 (265.5)	960.5 (295.5)	993.1 (325.2)	912.1 (267.7)	950.8 (299.0)	< 0.001	> 0.05	< 0.001	> 0.05	< 0.001

p values < 0.05 indicate statistical significance

in wall thickness due to hyperostosis caused by chronic rhinosinusitis reduced sinus volume. The increase in PPF volume in patients with mucosal thickening of the sphenoid sinus can be explained by the same mechanism [16].

Yonetsu et al. [38] reported that the volume of the sinus sphenoidalis increased up to the third decade of life and then decreased in volume with increasing age. They also stated that problems in sinus aeration caused a decrease in the volume of the sinus. The decrease in sinus volume and increase in PFF volume observed in the current study supports the studies by Moss and Salentijn [24] and Dargaud et al. [6].

Hwang et al. reported that in the Le Fort I procedure, the osteotomy margin should be located 2–3 mm anterior to the PMF and that the likelihood of fracturing the pterygoid plates was higher in the presence of a thin pterygomaxillary region and a deeply concave PMF. They noted that this may cause hemorrhage from the maxillary artery and emphasized the necessity of preoperative CT evaluation of the region [13]. Lima et al. reported that in patients with short and poorly fused pterygomaxillary junctions, the risk of pterygoid plate fracture during Le Fort I osteotomy is lower, as is the chance of damage to the structures passing through the PPF [18]. Moreover, Cruz and dos Santos reported that blindness was one of the ophthalmic complications of Le Fort I osteotomy, stating that opposing forces transmitted to the skull base via the sphenoid bone during pterygomaxillary separation can cause this complication. They emphasized that pterygomaxillary separation was the most critical step of the Le Fort procedure and that it must be performed with great care. They asserted that surgeons should ensure that the pterygoid plates are completely separated to avoid any unwanted maxillary mobilization and skull base complications, such as damage to the optic and other cranial nerves or the internal carotid artery branches [5]. Based on our study, we believe that the risk of complications is lower with shorter dimensions and volumes of the PMF and PPF area.

Detailed examination and PMF anatomic variations identified in the present study may be beneficial in the diagnosis and treatment of trigeminal neuralgia.

Stajcić et al. reported that in cases requiring anesthesia of the maxillary nerve in the PPF, the administration of extraoral anesthesia is difficult if the PMF width is less than 2 mm or if the sphenoidal process morphology prevents the needle from entering the PMF [30]. In the presence of any of these anatomic variations or any pathological condition that would prevent anesthesia administration through the PMF, injection into the PPF through the pterygopalatine canal is an alternative [21]. Acar et al. reported that PMF length did not differ greatly in their study, whereas the PMF width was highly variable. They noted that the superior part of the PMF was widest, and the upper part was therefore more suitable when entering the PPF. They also observed a positive

Table 4 Comparison of PMF areas according to age

Age groups (years)	Right PMF coronal area, mean mm (SD)	*p* value	Left PMF coronal area, mean mm (SD)	*p* value	Right vs. left
18–30 (a)	88.7 (27.8)	**a–c, d, e, f, g**	88.7 (29.6)	**a–c, d, e, f, g**	$p < 0.001$
31–40 (b)	94.2 (30.5)	> 0.05	94.2 (32.2)	$p > 0.05$	$p < 0.001$
41–50 (c)	102.7 (31.5)	**c–a**	101.5 (32.0)	**c–a**	$p < 0.001$
51–60 (d)	106.5 (29.6)	**d–a**	104.5 (29.6)	**d–a**	$p < 0.001$
61–70 (e)	107.2 (30.0)	**e–a**	108.4 (29.9)	**e–a**	$p < 0.001$
71–80 (f)	107.7 (32.7)	**f–a**	109.5 (31.4)	**f–a**	$p < 0.001$
81–91 (g)	108.4 (36.8)	**g–a**	109.9 (33.3)	**g–a**	$p < 0.001$
Age groups (years)	Right PMF sagittal area, mean mm (SD)	*p* value	Left PMF sagittal area, mean (SD)	*p* value	Right vs. left
18–30 (a)	90.9 (25.3)	**a–c, d, e, f, g**	91.0 (25.4)	**a–c, d, e, f, g**	**$p < 0.001$**
31–40 (b)	94.9 (26.2)	> 0.05	94.8 (23.3)	$p > 0.05$	**$p < 0.001$**
41–50 (c)	95.2 (26.5)	**c–a**	95.0 (23.8)	**c–a**	**$p < 0.001$**
51–60 (d)	99.7 (25.6)	**d–a**	98.8 (23.3)	**d–a**	**$p < 0.001$**
61–70 (e)	101.4 (24.0)	**e–a**	101.5 (22.3)	**e–a**	**$p < 0.001$**
71–80 (f)	103.3 (25.5)	**f–a**	103.6 (29.3)	**f–a**	**$p < 0.001$**
81–91 (g)	103.9 (19.6)	**g–a**	104.1 (22.4)	**g–a**	**$p < 0.001$**
Age groups (years)	Right PMF axial area, mean mm (SD)	*p* value	Left PMF axial area, mean mm (SD)	*p* value	Right vs. left
18–30 (a)	88.2 (24.8)	**a–c, d, e, f, g**	85.6 (23.4)	**a–c, d, e, f, g**	**$p < 0.001$**
31–40 (b)	89.4 (25.5)	> 0.05	87.9 (24.2)	$p > 0.05$	**$p < 0.001$**
41–50 (c)	95.0 (25.7)	**c–a**	92.2 (26.1)	**c–a**	**$p < 0.001$**
51–60 (d)	95.9 (25.9)	**d–a**	92.8 (26.6)	**d–a**	**$p < 0.001$**
61–70 (e)	97.8 (30.2)	**e–a**	93.6 (27.2)	**e–a**	**$p < 0.001$**
71–80 (f)	99.2 (32.1)	**f–a**	96.5 (28.4)	**f–a**	**$p < 0.001$**
81–91 (g)	100.9 (32.7)	**g–a**	100.6 (30.2)	**g–a**	**$p < 0.001$**
Age groups (years)	Right PPF volume	*p* value	Left PPF volume	*p* value	Right vs. left
18–30 (a)	820.2 (246.5)	**a–c, d, e, f, g**	805.2 (282.5)	**a–c, d, e, f, g**	**$p < 0.001$**
31–40 (b)	921.5 (321.5)	**> 0.05**	899.7 (297.5)	$p > 0.05$	**$p < 0.001$**
41–50 (c)	949.5 (271.0)	**c–a**	940.7 (294.0)	**c–a**	**$p < 0.001$**
51–60 (d)	1000.1 (289.8)	**d–a**	993.8 (305.2)	**d–a**	**$p < 0.001$**
61–70 (e)	1065.7 (315.1)	**e–a**	1040.2 (309.7)	**e–a**	**$p < 0.001$**
71–80 (f)	1073.7 (321.7)	**f–a**	1050.4 (322.4)	**f–a**	**$p < 0.001$**
81–91 (g)	1170.4 (368.2)	**g–a**	1190.3 (333.3)	**g–a**	**$p < 0.001$**

p values < 0.05 indicate statistical significance. Bold letters indicate statistical significance among age groups

relationship between PMF length and width, a particularly important consideration in anesthesia and surgical oncology [1].

Radiological evaluations have allowed the craniofacial skeletal morphology to be studied for many years. However, conventional techniques are only useful for 2D evaluation of the 3D maxillofacial system. The introduction of 3D imaging methods has brought significant improvements in the areas of diagnosis and treatment. Compared to CT, the CBCT technique offers a lower dose of radiation, greater availability, easy and fast images, low cost, and high image quality [17, 23, 29, 36]. CBCT is an imaging technology that is developing day-by-day, and it provides a great advantage in dental imaging. It is necessary to apply the technology responsibly, using the lowest possible radiation doses [10]. However, in routine use, the radiation dose administered by CBCT remains controversial. The normally accepted radiation dose received by an individual is 1 mSv per year (1000 μSv). A significant amount of radiation from natural sources and the external environment is taken into a normal human body, and a relatively small portion is from medical purposes. According to the National Council on Radiation Protection (NCRP) report (1987), the annual per-capita radiation dose received from

nature in the United States is 300 (3 msv). Even radiation at this dose has not threatened human health [35].

Normal exposure yields approximately 60 mRem (0.6 mSv = 600 µSv) per year from medical, commercial, or industrial radiation, of which approximately 40 mRem, corresponding to a radiation level of 600 µSv, comes from medical radiation for diagnostic purposes. In our study, approximately 50 µSv radiation was applied during CBCT; this amount is much lower than that delivered by medical CT used to obtain such 3D images [35].

In recent years, the use of CBCT for 3D imaging in the evaluation of the maxillofacial region has increased due to the high amount of radiation received by patients during CT scans and the higher space requirement and cost of CT. In this regard, CBCT can be a powerful tool to evaluate maxillofacial and skull base anatomy [4, 8, 9, 34].

This study aimed to investigate the detailed anatomy of the PMF and PPF and variations in that anatomy. The clinical relevance of this study lies in its detailed evaluation of the structures of the PMF and PPF. The anatomy can influence the success of anesthesia or a maxillary nerve block for trigeminal neuralgia patients. Thus, knowing the exact anatomy prior to the procedure is particularly helpful for clinicians during guided nerve blockage using CBCT or CT guidance.

Summary

In summary, the PMF area and PPF volume increase with age. Assessment of the shape, area, and volume of certain anatomical structures before any surgical intervention may provide guidance that will help to minimize complications. A wide PMF facilitates pterygomaxillary separation using osteotomes during maxillofacial surgery; however, knowledge of these anatomical variations will allow the surgeon to adjust the osteotome angle to avoid damage to the neurovascular structures passing through the area.

Author contributions KO and MI: project development, data collection, and manuscript writing. MI: data collection and manuscript editing. MI and KO: data analysis.

Funding There was no funding in this study.

Compliance with ethical standards

Conflict of interest The authors declare that they have no conflict of interest.

References

1. Acar R, Şakul BU, Türkaslan A, Ercan MA (1991) Fissura pterygomaxillaris (Sphenomaxillaris)'in şekil varyasyonları ve bunun klinikteki önemi. Ankara Tıp Mecmuası 44:537–544
2. Arai Y, Tammisalo E, Iwai K, Hashimoto K, Shinoda K (1999) Development of a compact computed tomographic apparatus for dental use. Dentomaxillofac Radiol 28:245–248
3. Bannon R, Parihar S, Skarparis Y (2018) 3D printing the pterygopalatine fossa: a negative space model of a complex structure. Surg Radiol Anat 40:185–191
4. Bou Serhal C, Jacobs R, Gijbels F, Bosmans H, Hermans R, Quirynen M (2001) Absorbed doses from spiral CT and conventional spiral tomography: a phantom vs. cadaver study. Clin Oral Implant Res 12:473–478
5. Cruz AAV, dos Santos AC (2006) Blindness after Le Fort I osteotomy: a possible complication associated with pterygomaxillary separation. J Craniomaxillofac Surg 34(4):210–216. https://doi.org/10.1016/j.jcms.2006.01.001
6. Dargaud J, Cotton F, Buttin R, Morin A (2003) The maxillary sinus: evolution and function in aging. Morphologie 87(276):17–22
7. Derinkuyu BE, Boyunaga O, Oztunali C (2017) Pterygopalatine fossa: not a mystery! Can Assoc Radiol J 68:122–130
8. Dula K, Mini R, Lambrecht JT, Van der Stelt PF, Sehneeberger P, Sanderink GCH (1997) Hypothetical mortality risk associated with spiral tomography of the maxilla and mandible prior to endosseous implant treatment. Eur J Oral Sci 105:123–129
9. Dula K, Mini R, Van der Stelt PF, Sanderink GC, Schneeberger P, Buser D (2001) Comparative dose measurements by spiral tomography for preimplant diagnosis: the Scanora machine versus the Cranex Tome radiography unit. Oral Surg Oral Med Oral Pathol Oral Radiol Endod 91(6):735–742
10. European Commission, Radiation Protection NO, 172 SedentexCT (2012) Guidelines on CBCT for dental and maxillofacial radiology. Luxembourg, EU publication office. https://ec.europa.eu/energy/sites/ener/files/documents/172.pdf. Accessed 15 Dec 2018
11. Evans BT (2016) Infratemporal and pterygopalatine fossae and temporomandibular joint. In: Standring S (ed) Gray's anatomy, 41st edn. Elsevier, Amsterdam, pp 534–555
12. Hitotsumatsu T, Matsushima T, Rhoton AL (1999) Surgical anatomy of the midface and the midline skull base. Oper Tech Neurosurg 2(4):160–180. https://doi.org/10.1016/S1092-440X(99)80017-6
13. Hwang K, Lee DK, Chung IH, Lee SI (2001) Le Fort I osteotomy with sparing fracture of lateral pterygoid plate. J Craniofac Surg 12:48–52
14. Justus J, Tuinzing DB, Greebe RB, van der Kwast WA (1991) Intra-and early postoperative complications of the Le Fort I osteotomy: a retrospective study on 410 cases. J Craniomaxillofac Surg 19(5):217–222. https://doi.org/10.1016/S1010-5182(05)80551-7
15. Kim HY, Kim MB, Dhong HJ, Jung YG, Min JY, Chung SK (2008) Changes of maxillary sinus volume and bony thickness of the paranasal sinuses in longstanding pediatric chronic rhinosinusitis. Int J Pediatr Otorhinolaryngol 72(1):103–108
16. Kim YH, Sato K, Mitani H, Shimizu Y, Kikuchi M (2003) Asymmetry of the sphenoid bone and its suitability as a reference for analyzing craniofacial asymmetry. Am J Orthod Dentofacial Orthop 124(6):656–662. https://doi.org/10.1016/S0889540603007716
17. Kumar V, Ludlow J, Soares Cevidanes LH, Mol A (2008) In vivo comparison of conventional and cone beam CT synthesized cephalograms. Angle Orthod 78(5):873–879

18. Lima SM Jr, de Moraes M, Asprino L (2011) Photoelastic analysis of stress distribution of surgically assisted rapid maxillary expansion with and without separation of the pterygomaxillary suture. J Oral Maxillofac Surg 69(6):1771–1775. https://doi.org/10.1016/j.joms.2010.07.035
19. Ludlow JB, Davies-Ludlow LE, Brooks SL (2003) Dosimetry of two extraoral direct digital imaging devices: NewTom cone beam CT and Orthophos Plus DS panoramic unit. Dentomaxillofac Radiol 32(4):229–234
20. Mah JK, Danforth RA, Bumann A, Hatcher D (2003) Radiation absorbed in maxillofacial imaging with a new dental computed tomography device. Oral Surg Oral Med Oral Pathol Oral Radiol Endod 96:508–513
21. Malamed SF, Trieger N (1983) Intraoral maxillary nerve block: an anatomical and clinical study. Anesth Prog 30(2):44–48
22. Moiseiwitsch J, Irvine T (2001) Clinical significance of the length of the pterygopalatine fissure in dental anesthesia. Oral Surg Oral Med Oral Pathol Oral Radiol Endod 92(3):325–328. https://doi.org/10.1067/moe.2001.115977
23. Moshiri M, Scarfe WC, Hilgers ML, Scheetz JP, Silveira AM, Farman AG (2007) Accuracy of linear measurements from imaging plate and lateral cephalometric images derived from cone-beam computed tomography. Am J Orthod Dentofac Orthop 132:550–560
24. Moss ML, Salentijn L (1969) The primary role of functional matrices in facial growth. Am J Orthod 55(6):566–577
25. Nish I, Pynn B, Holmes H, Young E (1995) Maxillary nerve block: a case report and review of the intraoral technique. J Can Dent Assoc 61(4):305–310
26. Puche-Torres M, Blasco-Serra A, Campos-Pelaez A (2017) Radiological anatomy of the fissura pterygomaxillaris for a surgical approach to ganglion pterygopalatinum. J Anat 231:961–969
27. Rhea JT, Novelline RA (2005) How to simplify the CT diagnosis of Le Fort fractures. AJR Am J Roentgenol 184(5):1700–1705. https://doi.org/10.2214/ajr.184.5.01841700
28. Scarfe WC, Farman AG, Sukovic P (2006) Clinical applications of cone-beam computed tomography in dental practice. J Can Dent Assoc 72(1):75–80
29. Silva MAG, Wolf U, Heinicke F, Bumann A, Visser H, Hirsh E (2008) Cone beam computed tomography for routine orthodontic treatment planning: a radiation dose evaluation. Am J Orthod Dentofac Orthop 133(5):640.e1–640.e5
30. Stajčić LS, Gačić B, Popović N, Stajčić Z (2010) Anatomical study of the pterygopalatine fossa pertinent to the maxillary nerve block at the foramen rotundum. Int J Oral Maxillofac Surg 39(5):493–496
31. Stechison MT, Brogan M (1994) Transfacial transpterygomaxillary access to foramen rotundum, sphenopalatine ganglion, and the maxillary nerve in the management of atypical facial pain. Skull Base Surg 4(1):15–20
32. Sukovic P (2003) Cone beam computed tomography in craniofacial imaging. Orthod Craniofac Res 6(Suppl 1):31–36
33. Tashi S, Purohit BS, Becker M, Mundada P (2016) The pterygopalatine fossa: imaging anatomy, communications, and pathology revisited. Insight Imaging 7:589–599
34. Thomas SL (2008) Application of cone-beam CT in the office setting. Dent Clin N Am 52(4):753–759
35. U.S.NRC (United States Nuclear Regulatory Commision) (2004) Biological effects on radiation. https://www.hsdl.org/?view&did=28420. Accessed 15 Dec 2018
36. van Vlijmen OJ, Bergé SJ, Swennen GR, Bronkhorst EM, Katsaros C, Kuijpers-Jagtman AM (2009) Comparison of cephalometric radiographs obtained from cone-beam computed tomography scans and conventional radiographs. J Oral Maxillofac Surg 67:92–97
37. William SC, Farman AG (2008) What is cone-beam CT and how does it work? Dent Clin N Am 52:707–730
38. Yonetsu K, Watanabe M, Nakamura T (2000) Age-related expansion and reduction in aeration of the sphenoid sinus: volume assessment by helical CT scanning. Am J Neuroradiol 21(1):179–182